Article

Ultrafast Dynamics in Cu-Deficient CuInS$_2$ Quantum Dots: Sub-Bandgap Transitions and Self-Assembled Molecular Catalysts

Published as part of The Journal of Physical Chemistry virtual special issue "125 Years of The Journal of Physical Chemistry".

Nora Eliasson, Belinda Pettersson Rimgard, Ashleigh Castner, Cheuk-Wai Tai, Sascha Ott, Haining Tian, and Leif Hammarström*

Read Online

ACCESS | Metrics & More | Article Recommendations | Supporting Information

ABSTRACT: The photophysical properties of Cu-deficient Cu$_{0.2}$In$_1$S$_x$ quantum dots synthesized through a facile aqueous-based procedure have been investigated. Transient absorption experiments were carried out probing in the UV−vis, near-IR, and mid-IR regions, with the aim to (i) study the photophysical properties of the quantum dots and (ii) monitor kinetics of electron transfer to a molecular catalyst. When pumping sub-bandgap transitions, negative (bleach) signals were observed that were spectrally and kinetically distinct from those observed with bandgap pump wavelengths. Herein, these distinct contributions are suggested to result from the overlapping bleaching of state filling electrons and trapped holes. Such an interpretation highlights the importance of considering the hole-contributions to the bleach for the proper determination of carrier kinetics in similar systems. A model complex of the [Fe$_2$]-hydrogenase active site was introduced to explore the potential of the quantum dots as photosensitizers for molecular catalysts. The quantum dot photoluminescence was quenched upon catalyst addition, and direct evidence of the singly reduced catalyst was found by transient absorption in the UV−vis and mid-IR. The catalyst accepted reducing equivalents on a subpicosecond time scale upon photoexcitation of the quantum dots, despite no covalent linking chemistry being applied. This implies that charge transfer is not limited by diffusion rates, thus confirming the presence of spontaneous quantum dot and catalyst self-assembly.
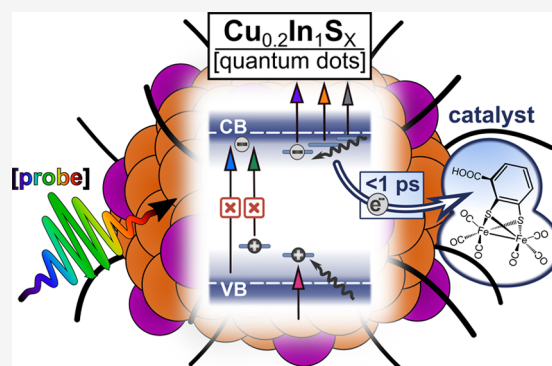
INTRODUCTION

In recent years, two key challenges have been on the agenda in science, technology, and politics: first, to meet the needs of a rising global energy demand resulting from population growth, the aspiration for equal human prosperity, and the increasing energy requirements of the richer population. Second, our planet has responded to the presence of human activities in disquieting ways, indicating that our excessive consumption of natural resources and release of greenhouse gas emissions, causing anthropogenic climate change, are not sustainable. From the variety of phenomena that nature offers to meet our needs, the direct harnessing of the sun's energy to form solar fuels could transform the way energy is supplied and thus contribute to resolve these challenges in a sustainable and renewable manner.[1−5]

Model systems to generate solar fuels are increasingly explored in the literature. In the field of photocatalysis, photons are used as the energy source to facilitate energetically *downhill* ($\Delta G < 0$) chemical reactions. From natural photosynthesis, nature has given us a blueprint for how the

principles of photocatalysis can be extended to drive energetically *uphill* ($\Delta G > 0$) reactions, allowing the sun's energy to be stored in chemical bonds for the future use as an energy source. A redox-driven photocatalytic system typically consists of two major components: (i) sensitizers acting as photo-oxidants/reductants by absorbing photons and generating free charge carriers and (ii) catalysts that can receive the redox equivalents and thus become catalytically active. Molecular catalysts (sometimes denoted cocatalysts) are suitable components to facilitate the preferred reactions, considering that they are small and tunable which can allow for fast and selective catalysis.[5] The efficiency of photocatalytic systems is partly dictated by the photosensitizer: its absorption
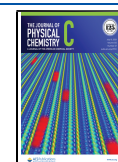
spectrum, excited-state lifetime, as well as the rate and nature of the interfacial charge transfer event.[6]

Quantum confined colloidal semiconducting nanocrystals, so-called quantum dots (QDs), have demonstrated intrinsic advantages in their photophysical properties to act as photosensitizers. The size-restriction of such small nanocrystals contributes significantly to the system properties, changing the carrier wave functions and surface conditions.[7,8] The most distinct property of QDs is the dependence of their electronic energies on the degree of spatial confinement. The result is a correlation between their crystalline size and bandgap energy, thus enabling synthetic tunability of their light-absorption range. The electronic confinement limits the allowed energies for electrons and holes; consequently, they display properties between bulk semiconductors and discrete atoms or molecules. On the downside, many of the explored systems rely on highly toxic heavy-metal-based QDs such as CdSe, CdS, or CdTe.[8−11] Ternary I−III−VI $CuInS_2$ (CIS) QDs are promising alternatives as they exhibit these favorable properties while relying on less toxic elements.

In general, the high surface-to-volume ratio of QDs results in the introduction of intrabandgap electronic states associated with dangling bonds on the surface, which might act as carrier traps. The ternary relatives of CIS, specifically, have also shown a high prevalence of trap states originating from lattice-strain and defects. However, their great tolerance toward compositional off-stoichiometry allows synthetic control over these states, adding yet another degree of freedom for tuning relevant properties.[12] The high surface area of QDs is also well-known to facilitate surface interactions.[7] Surface ligands are often used to control the growth of the nanocrystals during synthesis, as well as to control solubility and surface states. In recent years, the focus has expanded to include the functionalization of the surface with agents that can participate in photocatalysis.[7,9,10,13,14] For example, a recent study showed that CIS QDs covalently linked with rhenium bipyridine molecular catalysts for CO_2 reduction resulted in ultrafast (<300 fs) catalyst reduction, as evidenced by the catalyst transient IR signals.[15] The reference system *without* any covalent linking between the QDs and the rhenium complex showed lower photocatalytic activity, but surprisingly, the ultrafast charge transfer kinetics was maintained. Similar ultrafast charge transfer events, without any designed anchoring groups, were also observed in another study using $CuInS_2$/ZnS QDs as photosensitizers for a CO_2 reducing, *meso*-tetraphenylporphyrin iron chloride catalyst.[16] In the latter, the authors provided indirect evidence of the ultrafast electron transfer (<200 fs) to the catalyst by the lower initial magnitude of the QDs ground state bleach in the presence of the catalyst.[16] These studies thus imply the presence of spontaneous self-assembly of the QD-catalyst complexes as these redox systems are not limited by diffusion rates. For the photocatalytic activity to be realized in an implemented system, the charge transfer to the catalyst has to be fast enough to prevent losses (e.g., recombination) and the lifetime of the charge-separated state has to be sufficiently long for the catalyst to facilitate the preferred reaction. The tunable excited-state lifetime of CIS QDs and the fast electron transfer kinetics of self-assembled systems therefore provide yet another motivation for exploring these QDs as photosensitizers in inorganic−organic hybrid systems for photocatalysis.

The present work has used spectroscopic tools, mainly transient absorption (TA) experiments, to obtain information about the photophysical properties of the Cu-deficient $CuInS_2$ QDs. In addition, TA experiments were used to probe kinetics of electron transfer from the CIS QDs to a [Fe_2]-hydrogenase active site model complex [Fe_2(cbdt)$(CO)_6$], where cbdt = 1-carboxylbenzene-2,3-dithiolate. The parent complex [Fe_2(bdt)$(CO)_6$] (bdt = benzene-1,2-dithiolate) is well-known to catalyze hydrogen evolution by accumulating two electrons which couple to two protons. These molecular catalysts have the advantage, compared to many other well-known alternatives, of not relying on rare-earth metals.[17,18] The catalyst was simply mixed with the CIS QDs suspended in *N,N*-dimethylformamide (DMF) to investigate the possibility of spontaneous self-assembly between the QDs and the molecular catalysts, which has been reported in similar systems.[15,16] In addition, the role of the catalyst as electron acceptor aided in the assignment of the TA spectral contributions. In this study, we combine the strengths of QDs and molecular catalysts and provide direct evidence of ultrafast catalyst reduction in QD-catalyst complexes. With this, we aim to highlight the potential of making hybrid systems for photocatalytic fuel formation relying on environmentally benign materials and procedures.

■ EXPERIMENTAL SECTION

Chemicals. The following chemicals and solvents were purchased from Merck/Sigma-Aldrich, if not otherwise stated, and were used directly without any purification: copper chloride ($CuCl_2 \cdot 2H_2O$), indium chloride ($InCl_3$), trisodium citrate dihydrate ($C_6H_3Na_3O_7 \cdot 2H_2O$), sodium sulfide ($Na_2S$), L-cysteine (97%), tetrabutylammonium iodide (TBAI), *N,N*-dimethylformamide (DMF, 99.8%), nitric acid (HNO_3, TraceMetal Grade, Fisher Chemical), hydrogen peroxide (H_2O_2, 30%), ICP standards are Cu (1000 mg/L) and In (10 mg/L) in 2% HNO_3 (PerkinElmer, Inc.), ICP grade water (PerkinElmer, Inc.).

Quantum Dot and [Fe_2(cbdt)$(CO)_6$]/[Fe_2(bdt)$(CO)_6$] Synthesis. The molecular catalysts ([Fe_2(cbdt)$(CO)_6$]/ [Fe_2(bdt)$(CO)_6$]) (cbdt = 1-carboxylbenzene-2,3-dithiolate/ bdt = benzene-1,2-dithiolate) were synthesized by A. Castner following a previously reported procedure.[19] The (cbdt) complex was isolated as the second red band by column chromatography.

$Cu_{0.2}In_1S_x$ (CIS) QD synthesis was performed following the procedure reported by Chen et al. with the moderate modifications suggested by Huang et al.[20,21] Their aqueous based method at low temperatures allows a facile and environmentally benign procedure for CIS QD synthesis. In short, the capping ligand L-cysteine (2.4 mg, 0.02 mmol) in water (17 mL) was mixed with $CuCl_2$ (6 mL, 0.006 mmol), sodium citrate (0.40 mL, 0.16 mmol), and $InCl_3$ (0.04 mL, 0.04 mmol) stock solutions (prepared as given by ref 21). Na_2S (0.062 mL, 0.062 mmol) was subsequently injected under magnetic stirring (300 rpm), and the reactant system was heated (94 °C, 300 rpm) for 40 min, with a ~10 min heat-up. After this, the solution was cooled quickly in a water bath and TBAI (1 mL) was added dropwise (~40 s) during stirring. The solution was left stirring at room temperature (30 min) and subsequently purified by centrifuging (15 min, 9600 rpm) the dispersion in the presence of ethanol (~40 mL). The purified QDs were redispersed in DMF (~2−4 mL, ~10^2 μM, pp S2− S3) and typically used within 1 week.

It should be noted that ref 21 reports a QD product with a single broad PL (SPL) band (~750 nm) and a low-intensity

PL tail contribution at ~550 nm. The much more pronounced 550 nm band observed herein can be related to the much shorter excitation wavelength used (herein 400 nm; ref Huang et al., 500 nm). A similar SPL product was, however, observed in some of the batches synthesized in this study. This single PL product also exhibited a slightly more pronounced ground state absorption (GSA) tail band (see Figure S2c) and a significant red-shift in the GSA TA bleach compared to the QDs with dual PL. These observations are consistent with a higher abundance of Cu^+ in less Cu-deficient CIS, as indicated by their slightly higher Cu to In $(Cu_{0.3}In_1S_x)$ relative content as determined by inductively coupled plasma (ICP); see below. The exact conditions controlling the product outcome have not yet been determined. For good reproducibility of the desired product, we recommend that the setup is prepared so that the rates of the cooling and addition of reactants are consistent from batch-to-batch preparation. When prepared under very similar conditions, the procedure could be repeated multiple (>10) times with good reproducibility (Figure S2a).

Quantum Dot Characterization. Transmission electron microscopy (TEM) was carried out in a JEOL JEM-2100F microscope equipped with a Schottky field-emission gun and ultrahigh resolution polepiece. The samples dispersed in DMF were deposited on a Cu TEM grid with carbon supporting films and then dried in air at room temperature. The microscope was operated at 200 kV. The TEM and high-resolution TEM (HRTEM) images were recorded by a bottom-mounted Gatan Ultrascan XP1000 camera. Scanning TEM (STEM) was also performed in the same microscope. The probe size and camera length used were 0.2 nm and 10 cm, respectively. Annular dark-field (ADF) and bright-field (BF) STEM images were simultaneously acquired by a JEOL ADF and a Gatan BF detector, respectively, through Gatan DigitalMicrograph.

The relative content of Cu and In $(Cu_{0.2}In_1S_x)$ in five different QD batches was quantified by inductively coupled plasma optical emission spectroscopy (ICP-OES, Avio 200, PerkinElmer, Inc.). The samples were digested in a HNO_3/H_2O_2 (1:1, 1 mL) mixture at 80 °C in a Biotage SPX microwave reactor (Uppsala University, Sweden). Prior to measurements, all samples were diluted to ~5% (v/v) HNO_3 with ICP grade water and filtered (25 μm). Calibration curves were obtained using commercial Cu and In (2% HNO_3) calibration standards (PerkinElmer, Inc.). $[Cu]_1 = 0.798$ mg/L, $[Cu]_2 = 1.068$ mg/L, $[Cu]_3 = 0.381$ mg/L, $[Cu]_4 = 0.231$ mg/L, $[Cu]_5 = 0.261$ mg/L, $[In]_1 = 6.291$ mg/L, $[In]_2 = 9.079$ mg/L, $[In]_3 = 3.068$ mg/L, $[In]_4 = 2.170$ mg/L, $[In]_5 = 2.105$ mg/L, $[Cu:In]_1 = 1:4.36$, $[Cu:In]_2 = 1:4.70$, $[Cu:In]_3 = 1:4.45$, $[Cu:In]_4 = 1:5.19$, $[Cu:In]_5 = 1:4.46$. Product 2 (see CIS QD synthesis, SPL): $[Cu]_{1,SPL} = 0.561$ mg/L, $[Cu]_{2,SPL} = 5.201$ mg/L, $[In]_{1,SPL} = 3.581$ mg/L, $[In]_{2,SPL} = 30.17$ mg/L, $[Cu:In]_{1,SPL} = 1:3.53$, $[Cu:In]_{2,SPL} = 1:3.21$. The results are summarized in Table S1.

Powder X-ray diffraction (PXRD) pattern was obtained using a Simons D5000 diffractometer ($\lambda = 1.5418$ Å, 45 kV, 40 mA) with a 20–80 2θ scan range and 0.02° step size.

Steady-State Optical Spectroscopy. All steady-state absorption measurements in the UV–vis/NIR (Varian Cary 50/Cary 5000, Agilent Technologies) were performed in DMF using a 10 mm quartz cuvette and baseline-corrected with a DMF blank. Photoluminescence (PL) and PL excitation (PLE) spectra were recorded on a Fluorolog-3 fluorimeter (Horiba Scientific) in a right-angle geometry. Quenching

experiments with CIS QDs and the $[Fe_2(cbdt)(CO)_6]/[Fe_2(bdt)(CO)_6]$ catalysts were performed at constant QD concentration with a QD absorption of ~0.04 at the excitation wavelength (560 nm).

Time-Resolved Optical Spectroscopy. All measurements were performed in DMF at ambient temperatures. Transient absorption (TA) experiments were carried out using a Ti:sapphire based amplifier with integrated oscillator and pump lasers. The laser fundamental (800 nm, 3 kHz) was split into pump and probe by a beam splitter, which were directed toward the UV–vis–NIR/MIR sample chambers (TAS, Newport Corp./Helios IR, Ultrafast Systems). The 400 nm bandgap pump was generated by frequency doubling of the amplifier output using a birefringent barium borate (BBO) crystal. All other pump wavelengths were obtained through optical parametric amplifiers (TOPAS-prime and TOPAS NirUVis, Light Conversion). Prior to the sample cell, the pump was passed through a depolarizer and attenuated using a neutral density filter.

In the UV–vis/NIR, the probe supercontinuum was generated from a calcium fluoride/sapphire (CaF_2/Al_2O_3) crystal and its path was controlled by an optical delay ($t_{window} \leq$ 8 ns), allowing the transient spectra at varying pump–probe delay times to be recorded on a silicon diode array (home-built, Newport custom-made). The instrument response function (IRF) was typically 130–150 fs, depending on the pump and probe wavelengths used. The samples were placed in quartz cuvettes (1 mm path length) and adjusted to a QD absorbance of ~0.1–0.6 at the excitation wavelength. The measurements were performed with pump powers ranging from 20 to 600 μW (~13–400 nJ/pulse) using bandgap pump wavelengths and 100–800 μW (~65–530 nJ/pulse) for sub-bandgap pump wavelengths.

In the MIR, the broadband MIR probe centered at 4900 nm (2040 cm^{-1}) was obtained by passing a TOPAS-prime coupled with frequency mixers (Light Conversion). Prior to reaching the sample, the probe beam was split into a probe and reference beam of equal intensity using a wedged ZnSe window. The pump intensity was attenuated by a neutral density filter to ~100 and ~800 μW for pump wavelengths of 400 and 560 nm, respectively. The IRF was approximately ~200 fs. A sample cell with a 650 μm Teflon spacer between two CaF_2 windows was used. For the QD–cat experiments in the UV–vis/NIR and MIR, the $[Fe_2(cbdt)(CO)_6]$ (0.2–1 mM) was added to the suspended QDs prior to measurement. All TA data sets were analyzed using SurfaceXplorer for background extraction and time-zero correction and for fitting the chirp to a third-order polynomial function. Initially, the individual scans were analyzed carefully for inconsistencies, showing no indication of photodamage of the QDs. This is further supported by the unaltered GSA spectrum of the CIS QDs after TA measurements (Figure S2a: inset). Global analysis was performed by least-squares fitting using the R package TIMP and its GUI Glotaran. A sum of exponentials with frequency dependent amplitudes were fitted to the transient data using a parallel scheme, yielding decay associated spectra (DAS).

Time correlated single photon counting (TCSPC) was recorded on two separate pieces of equipment (separated with "/") using a pulsed diode laser source (Edinburgh Instruments EPL404/Horiba Instruments Inc. NanoLED) operating at 404.7/315 nm. The time-to-amplitude converter (TAC) was set to a 1/1.6 μs time range over 4096 channels. For technical
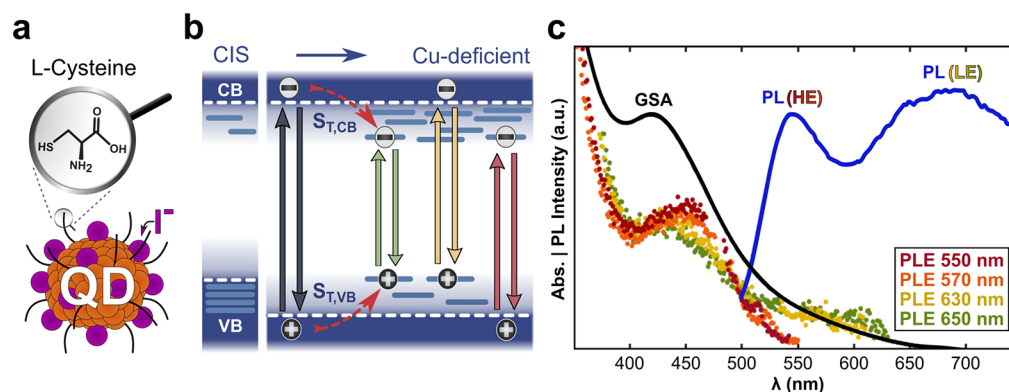
Figure 1. (a) Illustration of the present $Cu_{0.2}In_1S_x$ quantum dots (QDs). (b) Schematic of absorption (solid arrow up) and photoluminescence (PL, solid arrow down) related to bandgap (gray solid arrows) optical transitions together with trapping pathways for the photogenerated CB electron and VB hole (red dashed arrows). The different possibilities for sub-bandgap optical transitions are depicted by green, yellow, and red solid arrows. Left side: stoichiometric $CuInS_2$ QDs. Right side: Cu-deficient $CuInS_2$ QDs. (c) Optical spectra for $Cu_{0.2}In_1S_x$ QDs: ground state absorption (GSA) and PL (HE, ~550 nm; LE, ~680 nm). PL excitation (PLE) spectra were monitored at different wavelengths. Regions with scattering contributions have been omitted from the PLE for clarity.

reasons, the 315 nm excitation source was used to monitor the wavelength dependence of the decay components, with the emission monochromator approximately centered at each of the two overlapping PL bands (HE $\lambda_{mon,550}$ and LE $\lambda_{mon,670}$). The obtained time components agree well with the 404.7 nm excitation source (Table S2), and no additional PL bands were observed. Colloidal Ludox (IRF estimation) and QD samples (QD/DMF) were measured using a 10 mm quartz cuvette in the reverse mode under magic angle polarization. A 450 nm cutoff filter was used to block scattered laser light. Fluorescence lifetimes were obtained by an algorithm allowing iterative reconvolution with the measured IRF, using Decayfit software (Fluorescence Decay Analysis Software 1.3, Fluo-rTools) written by Dr. Søren Preus.

RESULTS AND DISCUSSION

Cu-Deficient $CuInS_2$ Quantum Dots. Following a previously reported aqueous based procedure, Cu-deficient CIS QDs were synthesized.[20,21] L-Cysteine was used as a capping ligand and TBAI as a surface passivation agent (Figure 1a). The synthesis resulted in crystalline QDs with a diameter of approximately 2−3 nm according to high-resolution and scanning transmission electron microscopy (HRTEM and STEM, respectively), as shown in Figure S1a−c. From HRTEM line-profile (Figure S1e) and powder X-ray diffraction (PXRD, Figure S1d), the QDs can be indexed to the chalcopyrite or zinc blende phase of $CuInS_2$ with a Cu:In ratio of ~1:5 ($Cu_{0.2}In_1S_x$) as determined by inductively coupled plasma (ICP) measurements (Table S1).

Previous studies on the photophysical properties of CIS QDs and their related ternary compounds have shown varying results due to their sensitivity to preparation method, where variations can be related to pH, reaction time, precursor stoichiometry, surface adsorbates, etc. The following experiments were repeated with good reproducibility on multiple QD batches within a week from synthesis.

Optical Characterization. The ground state absorption (GSA), photoluminescence (PL), and PL excitation (PLE) spectra of a representative batch of the CIS QDs in DMF are presented in Figure 1c (for additional batches see Figure S2a). The GSA spectrum shows a lower amplitude tail absorption (~470−650 nm) and a more prominent excitonic feature

(~400−470 nm) compared to their stoichiometric relatives. These observations are in accordance with previous results on Cu-deficient CIS QDs as well as off-stoichiometric examples of their ternary relatives.[22,23] A broad and featureless low-amplitude absorption is also present in the near-IR (NIR) region (Figure S2b). Dual PL (~550 nm, ~680 nm) bands are observed exciting with energies corresponding to the valence band−conduction band (VB−CB) excitonic transition. The PLE spectra monitored at the higher energy (HE) PL ($\lambda <$ 600 nm, red/orange dotted) band show a steep rise at around 500 nm toward lower wavelengths but resemble the GSA spectrum at energies related to exciton formation. Monitoring at the lower energy (LE) PL ($\lambda >$ 600 nm, yellow/green dotted) band results in PLE spectra with similar features in the blue spectral region and an additional tail contribution at lower energies.

Time-correlated single photon counting (TCSPC) was used to estimate the rates associated with the deactivation of the excited state. The QDs were excited with a pulsed diode laser operating above the bandgap energy (<400 nm). The decay profile of the full PL region (Figure S2d) was fitted with a three-exponential function reconvoluted with the IRF ($\tau_1 \sim 10$ ns, $\tau_2 \sim 50$ ns, and $\tau_3 \sim 200$ ns). Selectively monitoring each PL band (Figure S2e) revealed that the τ_2 component dominates the HE band ($\lambda_{mon,550}$, $A_{\tau1}$ [~0.3] < $A_{\tau2}$ [~0.7]) whereas τ_1 is weighted toward the LE band ($\lambda_{mon,670}$, $A_{\tau1}$ [0.75] > $A_{\tau2}$ [0.25]). The modest τ_3 contribution (<0.05: HE and LE) cannot be associated with any specific band; see the Experimental Section and Figure S2d,e and Table S2 in the Supporting Information for more details.

Stoichiometric CIS QDs (Cu:In, 1:1) often have a broad and featureless GSA spectrum, in contrast to QDs of other atomic compositions which often exhibit prominent GSA features from exciton generation.[22,24,25] The lack of a prominent excitonic feature in CIS compared to other QDs has been explained by a high prevalence of different localized Cu-based orbitals constituting the VB edge and delocalized electrons in a manifold of excited states.[23,26] In Cu-deficient CIS, the Cu-vacancies (related to the lower number of VB edge Cu(3d) orbitals) result in a higher Cu^{2+}/Cu^+ ratio to compensate for the charges.[26,27] The weak tail absorption in Cu-deficient CIS can therefore be associated with the lower
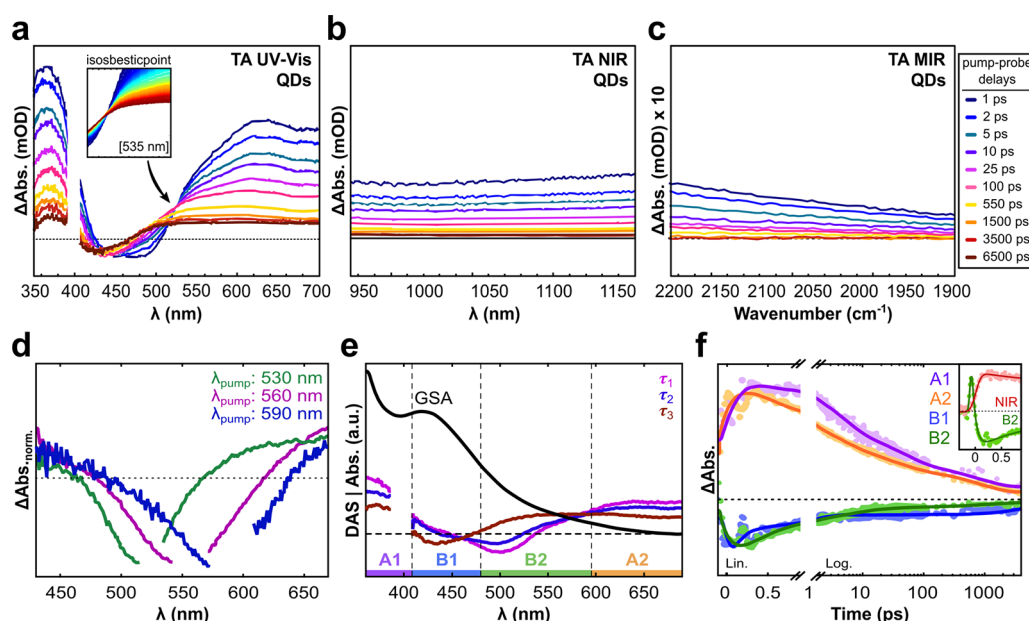
Figure 2. Difference spectra recorded by transient absorption (TA) experiments (pump, 400 nm; ~47 μJ cm^{-2}, $\langle N_{abs/QD} \rangle$ = 0.06) of Cu$_{0.2}$In$_1$S$_x$ quantum dots (QDs) probed in the (a) UV−vis, (b) NIR, and (c) MIR. The corresponding pump−probe delay times are shown in the box to the right of (c). (d) TA spectra (~1 ps) of Cu$_{0.2}$In$_1$S$_x$ QDs obtained using sub-bandgap pump energies. The pump scattering is removed from each spectral profile (white cut-out). (e) QD ground state absorption (GSA, black solid) spectrum and decay associated spectra (DAS) obtained from global analysis of the data presented in (a). The DAS represent the spectral dependence of τ_1 (~4 ps), τ_2 (~60 ps), and τ_3 (>8 ns). Different wavelength regions (A1, B1, B2, and A2) are color coded. (f) Single wavelength kinetics (spheres) with fits (solid lines) extracted from the A1, B1, B2, and A2 regions. Inset: NIR and B2 kinetics on the sub-ps time scale.

abundance of absorption active Cu$^+$-states close to the VB edge compared to stoichiometric CIS (right vs left side in Figure 1b). Cu^{2+}, on the other hand, is not considered optically active in the visible region.[27] As a result, the observed GSA (Figure 1c) features might stem from an effective lowering of the VB edge compared to stoichiometric CIS, resulting in a blue-shifted excitonic peak and a lower energy tail involving intrabandgap gap states. In Figure 1b, Cu$^+$ and related hole (S$_{T,VB}$) and electron (S$_{T,CB}$) trap states are shown schematically together with VB−CB excitonic (bandgap) transitions and possible tail-related optical transitions (absorption and PL). Due to the complex and debated nature of the states involved in the photophysical behavior of CIS QDs, we henceforth apply a simplified model where S$_{T,VB}$ and S$_{T,CB}$ in general correspond to undefined localized states.

Most commonly, a single broad and asymmetric PL with a long lifetime and large apparent Stokes shift is observed for CIS QDs. In several reported cases, however, more distinct contributions sometimes appear as shoulders and/or more separate bands.[28−31] The PL kinetics is usually multi-exponential and excitation wavelength-dependent involving both radiative and nonradiative recombination pathways.[32] Different models have been explored in the literature which attempt to provide an explanation for the unusual PL behavior in CIS QDs and their relatives, e.g., ternary I−III−VI$_2$ QDs and Cu-doped colloidal QDs. The most widely discussed contributions involve one or two carriers (i.e., electron/hole) localizing on CB/VB related trap states prior to recombination, as depicted by the red dashed arrows in Figure 1b.[25−27,33−35] The possible explanations for multiple PL bands and Stokes shifts includes competitive pathways involving band edge carriers and/or carriers trapped on intrabandgap states of varying nature as well as QD ensemble inhomogeneity due to Ostwald ripening and compositional differences.[22,29,31,34,36,37]

Off-stoichiometry significantly affects the PL behavior, where Cu deficiency has been shown to increase the PL quantum yield (Φ) and the excited state lifetime and to result in a blue-shift of the PL maximum.[30,34,37,38] The increase in Φ compared to stoichiometric CIS has previously been related to the higher abundance of Cu^{2+} in Cu-poor samples, where the associated Cu vacancies or alternative trap states efficiently accept the photogenerated holes from the VB, suppressing competitive higher energy recombination, and thus allows the electrons to recombine radiatively with permanent Cu^{2+} holes on longer time scales.[27,34] For samples dominated by Cu$^+$, hole-trapping by other than Cu$^+$ is detrimental to the PL yield and lifetime since this site requires activation to form a Cu^{2+}-like state prior to recombination.[27]

The dual PL bands observed herein could originate from competing pathways within the same QD ensemble or different subsets (i.e., chemical species), such as the coexistence of Cu-doped (Cu$_x$In$_x$S$_x$) and undoped (In$_x$S$_x$) QDs resulting from the large precursor Cu deficiency. Other binary contaminants such as Cu$_x$S could also be present as synthetic byproducts. The single phase observed in the XRD (Figure S1d), however, does not indicate any phase impurities from multiple crystalline contributions. Furthermore, STEM and HRTEM measurements (Figure S1a−c) reveal a relatively narrow size distribution and no obvious sample inhomogeneity. Binary products are therefore neglected in further analysis and the dual PL is considered to be intrinsic to the present type of QDs. It should be noted, however, that variations in the trap state nature of individual QDs might result in the formation of different subsets with a characteristic excited state behavior.

The distinctly different appearance of the PLE (Figure 1c) spectra when monitored at the HE (~550 nm) and LE (~680 nm) PL band, respectively, suggests that at least two different luminescent mechanisms are involved in the present QDs. The
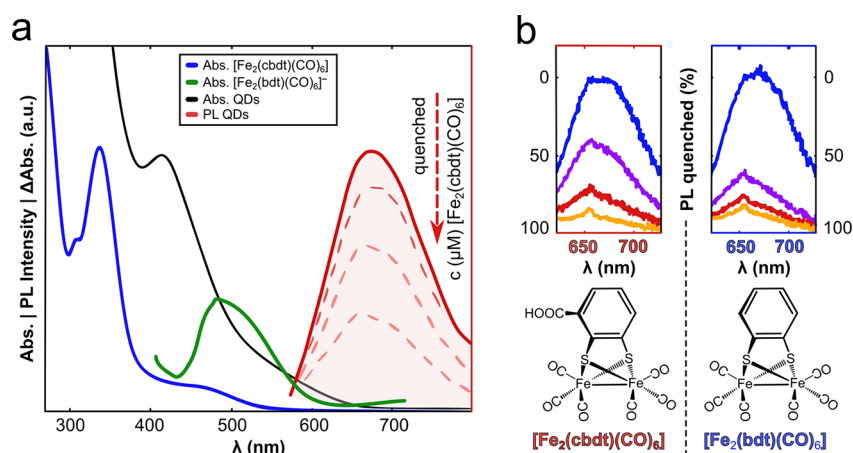
Figure 3. (a) Ground state absorption of $Cu_{0.2}In_1S_x$ quantum dots (QDs, black), $[Fe_2(cbdt)(CO)_6]$ catalyst (blue), and the photoluminescence (PL) of the QDs (red solid). The quenched PL upon increasing catalyst concentrations are shown with red dashed lines, where the decreasing PL corresponds to c_{cat} of 30, 50, and 80 μM with relative QD to catalyst ratios roughly estimated to 1:3 to 1:30, 1:5 to 1:50, and 1:8 to 1:80, respectively. See pp S2−S3 for [QD] estimation. The absorption from the singly reduced $[Fe_2(bdt)(CO)_6]^-$ parent compound, as reported in ref 41, is presented schematically (green). (b) Quenching experiments comparing the carboxylated $[Fe_2(cbdt)(CO)_6]$ complex with the $[Fe_2(bdt)(CO)_6]$ parent compound at identical quencher concentrations.

excitonic feature (∼400−470 nm) is present in all PLE spectra, indicating that both mechanisms are susceptible to bandgap excitations (gray solid arrow), which implies some degree of carrier localization to be a requisite for the LE recombination (red dashed arrows, Figure 1b). From monitoring at the LE band, the resulting tail in the PLE spectrum below the band edge can be attributed to the Cu⁺-to-CB transitions, which is consistent with our GSA assignment and TA observations (see below). From the energetic difference between the excitonic (∼bandgap) maximum and the tail band, these states can be estimated to extend roughly ≤650 meV above the VB edge. Furthermore, the TA experiments indicate a long-lived CB-population (>8 ns) upon both bandgap and sub-bandgap pumping, whereas no obvious rise is visible in the TCSPC PL trace on the nanosecond time scale. These results argue against substantial trapping of CB *electrons* to form the fluorescent states and suggest at least one luminescent recombination pathway that involves the CB edge. On the basis of this, we conclude that the two most likely mechanisms (Figure 1c) responsible for the dual PL bands in the present QDs can be associated with CB electrons recombining with trapped holes (yellow arrow) combined with (i) a band edge recombination (gray arrow) and/or (ii) trapped electrons to the VB (red arrow). One may also argue that the Stokes shift (∼550 meV) observed for the HE band is too large compared to the ∼100 meV that is commonly reported for bandgap recombination in QDs.[36] It should be noted, however, that in CIS QDs such an observation is not compelling evidence in favor of option ii, since large Stokes shifts can be explained by a phonon-assisted transition mechanism without involving intrabandgap states.[36]

Transient Absorption Measurements. The excited state behavior of CIS QDs dispersed in DMF was monitored by fs-TA experiments recording difference spectra at varying pump−probe delays. The pump fluence was kept within the linear regime where the number of absorbed photons per QD, $\langle N_{abs/QD} \rangle$, is ≪1, as shown in the Supporting Information (supporting calculations and Figure S3a) together with additional data and fits (Figures S4−S6 and Table S2). In general, minor variations are observed related to different QD batches and measurements; however, the TA magnitude and

the spectral dependence of the time components are retained with good similarity through all fitted spectra.

Selective excitation at different pump wavelengths was used to study the carrier dynamics following such transitions. First, difference spectra were recorded probing in the UV−vis, NIR, and mid-IR (MIR) regions using a 400 nm (above bandgap) pump. The resulting TA spectra can be summarized in two distinct features: (i) broad positive signals covering large parts of the probed regions (Figure 2a−c) and (ii) a negative feature in the visible which gets more narrow with increasing probe delay and prevails in the blue spectral region (Figure 2a). When using a 350 nm pump (Figure S4a), the TA spectral shapes and dynamics were similar to those using a 400 nm pump. Sub-bandgap excitation energies, however, result in distinctly different responses, as observed in Figure 2d. The most pronounced negative signal instead appears spectrally close to the pump at the tail band observed in the GSA. It should be noted that the negative feature does not cover the entire GSA tail region and that its center is different for the different pump wavelengths (530−590 nm).

The TA spectral evolution with time in the UV−vis and NIR (Figure 2a,b) was successfully fitted globally using a three-exponential model with associated time components of ∼4 ps (τ_1) and ∼60 ps (τ_2) and a long-lived contribution similar to/exceeding the time-window of the experiment, i.e., 8 ns (τ_3). Sub-ps contributions were not considered in the global analysis due to the contamination from time-zero artifacts. Single wavelength analysis (see below), however, provides complementary information on ultrafast processes. The obtained decay associated spectra (DAS) of the data shown in Figure 2a are presented in Figure 2e. The DAS represent the spectral dependence of $\tau_1 − \tau_3$, interpreted as loss or gain in absorption. The first and second DAS (τ_1 and τ_2, respectively) have similar shapes, showing a clear loss of the positive bands in the high and low energy spectral regime (A1, <400 nm and A2, >600 nm, respectively), as well as a recovery of the *lower* energy regime of the negative band (B2, 470−600 nm). The third and long-lived DAS (τ_3), on the other hand, dominates the negative band at shorter wavelengths (B1, 400−470 nm) and the positive signals. Single kinetic traces are presented in
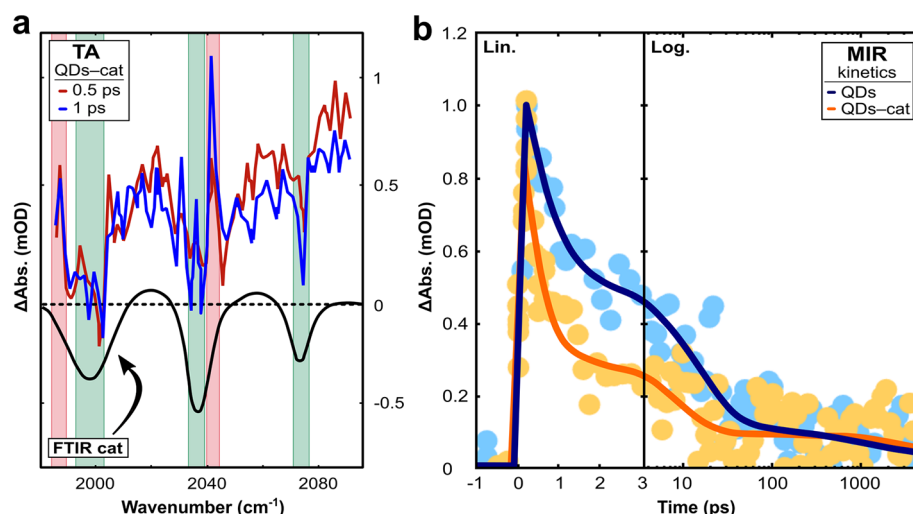
Figure 4. Transient absorption (TA) experiments probing $Cu_{0.2}In_1S_x$ quantum dots (QDs) mixed with $[Fe_2(cbdt)(CO)_6]$ catalyst (cat) in the mid-IR (MIR) using a 560 nm sub-bandgap pump. (a) Transient spectra (0.5 and 1 ps) of QDs−cat and the Fourier-transformed IR (FTIR) spectrum of the catalyst (black). The TA spectra show sharp negative (2074, 2037, and 2002 cm^{-1}, shaded green) and positive ($\sim$2042 and $\sim$1980 cm^{-1}, shaded red) features superimposed on the QD transient (offset). (b) Single trace kinetics extracted at 2100 cm^{-1}, showing a steeper decay of the QD-electron (offset) signal in QDs−cat (orange) compared to neat QDs (blue).

Figure 2f, where the time evolution at sub-ps times is visible in the leftmost part of the figure. It should be noted that the time-components obtained from fitting these very early time scales vary slightly between different measurements and probe wavelengths. Comparing the dynamics of the negative bands, however, reveals a sub-ps growth (i.e., increase in magnitude) of the B2 band, whereas the growth of the B1 band is limited by the time resolution of the measurement. On the other hand, a $\sim$0.5−1 ps recovery component is present in the early time B1 kinetics, in addition to the long-lived (>8 ns) component resolved in the DAS. The different dynamic behavior of the B1 and B2 band implies that they do not have a common origin. Furthermore, A1 and A2 show two distinct rise times, where A1 increases in magnitude up to $\sim$0.4−0.8 ps and A2 up to $\sim$0.3 ps. These observations will be discussed in more detail later, drawing also on the results with addition of catalyst.

Quantum Dots with Molecular Catalysts. Photodriven electron transfer from $Cu_{0.2}In_1S_x$ QDs to the $[Fe_2(cbdt)(CO)_6]$ catalyst should be thermodynamically favorable considering that the reduction potential for bulk $CuInS_2$ is −1.7 V vs SCE and increasingly negative for nanocrystals.[16] Weiss and co-workers estimated the reduction potential for stoichiometric $CuInS_2$ to −2.4 V vs SCE, i.e., approximately −2.8 V vs ferrocenium/ferrocene (Fc$^{+/0}$) for QDs with a diameter of 2.5 nm.[16,39] The reduction of $[Fe_2(cbdt)(CO)_6]$ occurs at an $E_{1/2}$ of −1.18 V vs Fc$^{+/0}$ which ensures a sufficient driving force for the electron transfer process (Figure 8).[40]

The charge-transfer event was first indicated by steady-state quenching experiments. The decreasing PL of the QDs with increasing catalyst concentration is shown in Figure 3a (red dashed lines) together with the GSA spectrum of the QDs (black) and of the catalyst (blue). For all measurements of the mixed QDs and catalyst system (QDs−cat), sub-bandgap excitation energies (560 nm) were used to excite the QDs to avoid significant absorption from the catalyst. The spectral overlap between the absorption band of the catalyst and the PL of the QDs is negligible, indicating that energy transfer is not a significant contribution to the observed quenching. Interestingly, quenching experiments performed with $[Fe_2(bdt)-$

$(CO)_6]$ (bdt = benzene-1,2-dithiolate) resulted in a higher degree of quenching, at identical concentrations, compared to the carboxylated compound primarily used in this study (left vs right column in Figure 3b). The significance of this observation will be discussed in more detail below.

Transient Absorption Measurements: Carrier Dynamics in Coupled Systems. The interfacial charge transfer from the QDs to the $[Fe_2(cbdt)]$ complex was investigated in more detail through fs-TA experiments probing in the UV−vis and in the MIR. MIR experiments were performed using a broadband probe centered at 4900 nm (2040 cm^{-1}). The difference spectra of the neat QDs (Figure S7a) show a broad positive feature (offset) typical for CB electrons, similar to the observation made using a bandgap pump (Figure 2c). Upon addition of the catalyst (Figure 4a), new sharp features can be observed on a sub-ps time scale (superimposed on the broad absorption) and they prevail during the full time-window of the measurement (Figure S7b).

The FTIR spectrum of the catalyst overlapped with the difference spectrum of QDs−cat is presented in Figure 4a. The sharp negative features at 2074, 2037, and 2002 cm^{-1} (shaded green) correspond to the bleaches of the three $[Fe_2(cbdt)(CO)_6]^0$ bands visible in the FTIR spectrum, originating from the carbonyl vibrational modes. Upon catalyst reduction, the C−O bonds are weakened as a result of back-donation from the metals to the antibonding molecular orbitals of the COs. Hence, the $[Fe_2]^0$ bands are bleached as the reduced species is formed. The concomitant appearance of two positive peaks at $\sim$2042 and $\sim$1980 cm^{-1} (shaded red) corresponds to two out of four of the expected $[Fe_2]^-$ bands, red-shifted compared to the two higher energy bleach bands by 30 and 55 cm^{-1}, respectively. The shift magnitude is typical for the singly reduced species of the $[Fe_2(bdt)(CO)_6]$ model complex and its carboxylated relative (the remaining bands are expected outside the probe region).[41,42] In a study by M. Pavliuk et al., they observed the singly reduced $[Fe_2(cbdt)]$ complex, bound to ZnO nanocrystals dispersed in dimethyl sulfoxide, at 2050 and 1985 cm^{-1} using ns-TA. This is in good agreement with
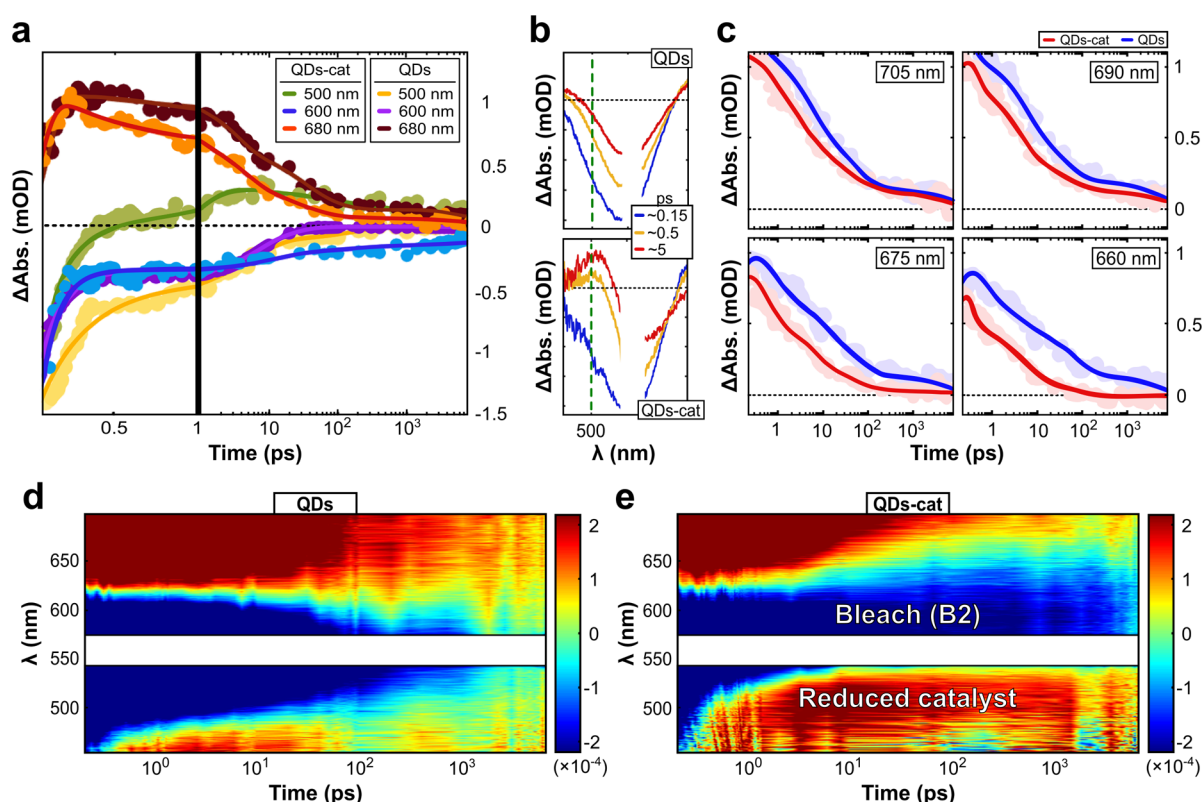
Figure 5. UV−vis transient absorption (TA) measurements (pump, 560 nm) comparing $Cu_{0.2}In_1S_x$ quantum dots (CIS QDs) and CIS QDs with $[Fe_2(cbdt)(CO)_6]$ catalyst (QDs−cat). (a) Single wavelength kinetics. (b) Close-up of TA spectra of QDs (top) and QDs−cat (bottom). The reduced catalyst absorbs at 500 nm (green dashed line). (c) Single wavelength kinetics of the QDs (blue) and QDs−cat (red) extracted from the positive transient (660−705 nm). The faster decay of the positive signal in the presence of the catalyst is more pronounced at shorter wavelengths (bottom right) and levels out toward the NIR (top left). 2D-maps (z-axis, ΔmOD) of the QD system (d) and QDs mixed with catalyst (e), probing in the UV−vis.

the current observation considering shifts related to solvents and the nature of the QD−catalyst interaction.[42]

Additionally, the QD background feature ($\tau_1 < 1$ ps, $\tau_2 \sim 15$ ps, and $\tau_3 \geq 8$ ns) decays faster in the presence of the catalyst (Figure 4b), as reflected in a significant increase in the relative weight of the sub-ps component, τ_1, as well as the concomitant lowering of the relative weight of the longer components, τ_2 and τ_3 (see Table S2 for details). This indicates that the broad signal involves electrons (e-CB or shallow trap states) that are transferred to the catalyst. The observed narrow IR features can therefore be assigned to the reduction of the catalyst. Note that the ~15 ps component was not observed in the CB edge population in the visible (B1 band) and can reflect additional processes such as hot carriers and/or intraband/trap states absorptions involving both electrons and holes.

As aforementioned, contributions from the excited catalyst are avoided by using sub-bandgap pump energies. Furthermore, an assignment of the TA to Stark shifted ground state bands is discarded based on (i) the quenched QD PL in the presence of the catalyst which indicates catalyst reduction, (ii) the faster decay of the MIR e⁻-signal (CB/traps) in the mixed system, and (iii) the magnitude of the spectral shifts of the appearing positive signals, which agree with literature data for the catalyst reduction.[41,42] Hence, these experiments reveal a sub-ps electron transfer to the catalyst, and a charge-separated state with a lifetime longer than the time-window of the instrument, i.e., >5 ns. This interpretation is further supported by the UV−vis TA experiments below.

In addition to probing in the MIR, UV−vis TA experiments of the coupled QD−cat system were performed in order to gain more information on the carriers involved in the interfacial electron transfer events from the QDs to the catalysts, as well as to facilitate the interpretation of the intrinsic QD dynamics. A 560 nm sub-bandgap pump was used for photoexcitation of the QDs, and the resulting TA spectra are presented in Figure 5b,d,e. First, a new positive feature appears in the QD−cat system (bottom graph in Figure 5b) at ~500 nm (green dashed line). This signal closely resembles the absorption feature of the singly reduced $[Fe_2(bdt)(CO)_6]$ model complex as observed in a previous study by M. Mirmohades et al. and depicted schematically in Figure 3a (green).[41] A comparison of single wavelength TA kinetics of the QDs and the QD−cat system is shown in Figure 5a, and the corresponding TA 2D-maps are in Figure 5d,e. At 500 nm, the trace from the QDs−cat system (green) shows a sub-ps rise of the appearing absorption feature. This signal is assigned to the superposition of the negative QD feature with the absorption from the reduced catalyst, in accordance with the observations made probing in the MIR. In addition, the negative B2 band remains for longer times in QDs−cat (blue) compared to neat QDs (violet). The positive A2 band, on the other hand, decays faster with the catalyst present (orange vs brown), which is also shown in Figure 5c (blue vs red) at different wavelengths of the A2 band.

Intrinsic Charge Carrier Dynamics. In the following sections we will discuss the data with the aim to present a model explaining the observed TA features and dynamics.
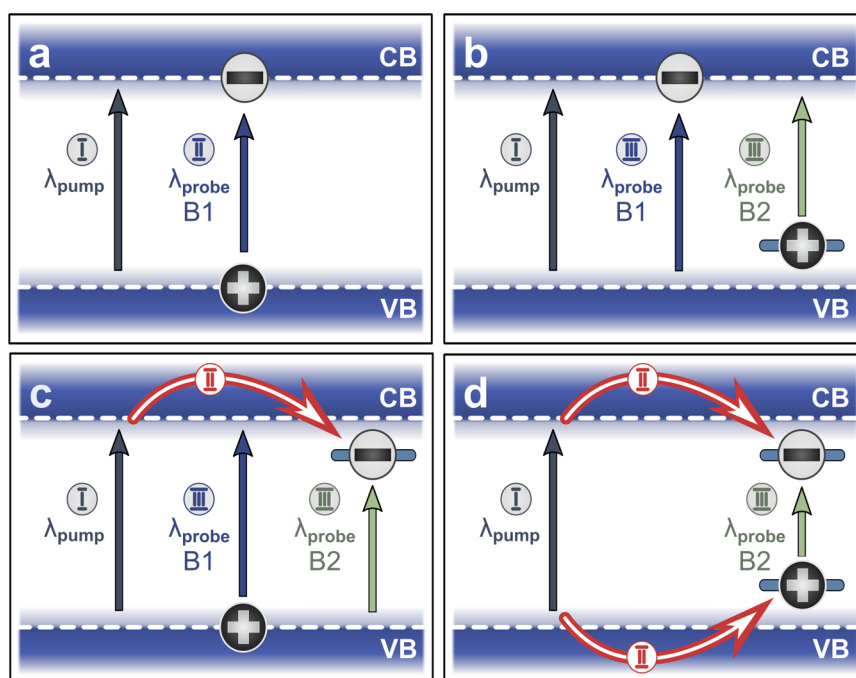
Figure 6. Schematic diagrams of charge carrier trapping and the resulting possibilities of transient absorption (TA) bleaching contributions. A pump-induced state of electrons in CB-related states and/or holes in VB related states can cause a bleaching of the optical transitions involving the occupied states. By use of a bandgap pump (λ_{pump}), the TA bleach shows two bands resulting from the reduced absorbance of bandgap (B1) and sub-bandgap (B2) transitions upon the arrival of the probe pulse. B1 can be associated with a state filling of the band edge states by (i) CB-electrons (a, b) and (ii) VB-holes (a, c). B2 can be associated with a state filling by (i) CB electrons and holes on VB-related trap states (b), (ii) electrons in CB-related trap states and VB holes (c), or (iii) both carriers trapping (d).

Bandgap and Sub-Bandgap Optical Transitions. Previous fs-TA studies of stoichiometric CIS QDs have revealed broad negative bands, similar to the featureless GSA often observed. Only a few spectroscopic studies have investigated Cu-deficient CIS QDs. Kamat and co-workers[22] compared CIS QDs and revealed two overlapping negative bands upon photoexcitation, similar to the observation made in this study. They noted that these bands were more distinct on samples with lower Cu/In ratio, revealing the dual presence of a bandgap bleach and a lower energy contribution resulting from the bleaching of sub-bandgap transitions.[22] A similar bleaching of sub-bandgap tail absorption was recently assigned by Klimov and co-workers[27] in CIS QDs and has also been observed in Cu-doped (Cu:CdSe/CdS) nanocrystals.[26,27] In the present study, the B1 (400−470 nm) band closely resembles the GSA spectrum (dark red vs black, Figure 2e), which is consistent with a state filling at the band edges. On the basis of this, a similar interpretation of overlapping bleaching from bandgap (B1) and sub-bandgap (B2) transitions is incorporated into the present model.

Electron vs Hole Contributions. A schematic diagram of charge carrier traps and the resulting possibilities of bleaching contributions for the B1 and B2 band upon bandgap pumping (λ_{pump}) is depicted in Figure 6a−c. A bandgap bleach can result from pump-induced state filling of the band edge states by (i) CB electrons (a, b) and (ii) VB holes (a, c). Importantly, a bandgap bleach (from state filling) cannot result from both carriers being trapped upon photoexcitation (d). The bleaching of sub-bandgap transitions, on the other hand, can be associated with a state filling by (i) CB electrons and holes on VB related trap states (b) or (ii) electrons in CB-related trap states and VB holes (c). A bleaching of sub-bandgap transitions can also result from both carriers trapping upon

photoexcitation (d). In previous studies of CIS QDs, the bleach has generally been assigned to a CB electron state filling induced bleach (a, b), where a contribution from the holes often is assumed to be negligible due to the higher density and degeneracy of the hole levels.[24,43]

In the present study, pump energies related to interband transitions (i.e., 350 and 400 nm) result in TA spectra with similar shapes and dynamics independent of the pump wavelength. This suggests that the carrier contributions to the signals following such transitions are similar in nature. In accordance with previous studies, we assign the major carrier contribution to the band edge bleach (B1) to the electron population in the CB (Figure 6a,b), which is consistent with the expected higher degeneracy and density of the VB compared to the CB.[24]

Signals related to electrons that are involved in the charge transfer event will disappear faster in the presence of the electron scavenger (catalyst), while those for holes will be more long-lived. A negative signal resulting from electron state filling (GSA bleach) or stimulated emission (SE) is therefore expected to recover with a time-component that can be associated with the catalyst reduction. When the QDs−cat system is pumped at 560 nm (sub-bandgap), the kinetics extracted at the lower energy tail of the negative B2 band (580−600 nm, blue trace in Figure 5a), which is not overlapping with the reduced catalyst absorption, show similar kinetics as the neat QDs (violet trace) at early times. In contrast, however, the negative band in QDs−cat (blue) remains during the full time-window of the measurement, whereas the bleach recovers completely in the absence of catalyst (violet).

From the sub-ps appearance of new spectral signals associated with the reduced catalyst in TA measurements

and from quenching experiments, one can conclude that the catalyst depletes electrons from the emissive state. Therefore, as sub-bandgap pump energies result in similar kinetics at initial times in the presence of the electron scavenger, neither SE nor state filling by electrons in CB related states (edge or traps) can be the major contribution to the negative B2 band. Instead, the band remains for longer times when adding the catalyst, which is a sign of the involvement of holes that recombine more slowly when the electrons are transferred to the catalyst.

Role of Trapped vs Band Edge Carriers. The experiments performed with the electron scavenger clearly indicate that, using sub-bandgap pump energies, the major contribution to the bleach dynamics is from the holes. Herein, we assign this contribution specifically to trapped holes. This assignment is evidenced by the two following observations. First, both interband (400 and 350 nm) and sub-bandgap (530–590 nm) pump energies result in TA difference spectra which exhibit a low-amplitude, long-lived spectral feature that resembles the B1 (400–470 nm) band superimposed on the positive A1 (<400 nm) signal (Figure S4,b,c). This suggests that sub-bandgap pump transitions involve an intrabandgap state *and* one of the band edges (or thermally coupled states), as depicted by the yellow and red arrows in Figure 1. This is in accordance with the assignment of the GSA tail to optically allowed sub-bandgap Cu^+-CB transitions (yellow arrow), where the holes which contribute to the B2 bleach dynamics reside on intrabandgap Cu ions and not the VB edge. Second, sub-bandgap pump energies result in a negative signal that is most pronounced spectrally close to the pump (Figure 2d). If the B2 bleach dynamics were reflecting only the involved band edge population, we would expect to observe bleaching at probe wavelengths roughly corresponding to the highest differential extinction coefficient between the ground and excited states and thus observe similar features independent of pump wavelength. The spectral shift of the bleach with sub-bandgap pump wavelengths therefore suggests that a trapped carrier is contributing to the bleach dynamics. Herein, we propose that the negative features observed using pump energies related to sub-bandgap transitions are dominated by the depletion of absorbing carriers (e.g., $Cu^+ \xrightarrow{h\nu, pump} Cu^{2+}$) in proximity to the VB edge.

By use of bandgap pump energies, the recovery kinetics of the B2 band clearly resembles the recovery kinetics using sub-bandgap pump energies, suggesting that these contributions are similar in nature and involve the hole population. A slight difference is observed at initial times, where a sub-ps increase in bleach magnitude is observed using bandgap pump energies (Figure 2f, green). This growth in B2 bleach magnitude is consistent with rapid localization of the photogenerated VB-holes to intrabandgap states ($S_{T,VB}$). Hence, as sub-bandgap transitions are sensitive to the hole population, an additional bleach at tail wavelengths (B2, ~470–600 nm) is observed. This is consistent with schematic b (and d) in Figure 6. With pump energies corresponding to sub-bandgap Cu–CB transitions, on the other hand, no obvious growth in bleach magnitude is observed since the holes do not have to localize prior to bleaching the transition. Our data are therefore consistent with the picture that bandgap and sub-bandgap optical transitions in the present QDs differ mainly in the nature of the involved hole states.

The present assignment contrasts the common assumption, specifically in stoichiometric CIS QDs, of a negligible contribution from holes to the bleach dynamics. Recently, however, Klimov and co-workers (2020) challenged this interpretation by assigning a fast decay component of the bleach associated with the VB–CB excitonic transition in Cu-poor CIS QDs to rapid hole localization.[27] The bleaching of sub-bandgap transitions, on the other hand, they attributed to the CB electron population in their QDs. To the best of our knowledge, no previous study of CIS or Cu-deficient CIS has shown a contribution from a trapped hole induced sub-bandgap bleach. The rationale for the presence of the hole-contribution in the present QDs is the lower density and isolated nature of the absorptive intrabandgap states introduced by the lack of copper in the crystal lattice. This is in accordance with the much lower tail amplitude in the GSA spectrum compared to their stoichiometric relatives. Thus, the role of the holes becomes more dominant in Cu-deficient CIS than in the limit of 1:1 (Cu:In) CIS. In the latter, a large manifold of absorptive Cu-related states (e.g., Cu^+) form a semicontinuum overlapping with the VB edge (Figure 1b) rather than being isolated states. The high density and degeneracy of the optically involved VB states might therefore render the hole contribution negligible, in a similar manner as for many other QDs. In CdSe QDs, the lack of the hole contribution to the band-edge bleach has been explained by the ultrafast removal of the holes from the VB-edge due to trapping.[44] In the present QDs, a subset of the associated hole-trap states have absorption transition strength, meaning that the hole removed from the VB can bleach these transitions.

Positive TA signals in the UV–vis/NIR are commonly observed in CIS QDs. In previous studies, these contributions have been assigned to (i) CB electrons, (ii) trapped electrons ($S_{T,CB}$) promoted to the CB, or to (iii) VB electrons promoted to VB related trap states ($S_{T,VB}$).[43,45−47]

The present QDs show prominent positive signals covering large parts of the probed regions (UV–vis/NIR/MIR). The presence of an electron contribution in the visible region is indicated by the following: from the kinetic traces presented in Figure 5a (brown vs orange), it is evident that the positive A2 signal in the visible decays more rapidly with the catalyst present (orange) than in the neat QDs (brown). In Figure 5c, it is clear that the faster decay of the positive signal in the presence of the catalyst (red vs blue) is more pronounced toward the higher energy region of the A2 band and levels out toward the NIR. The faster decay of the A2 signal at shorter wavelengths (~600−670 nm) appears to occur on similar time scales as the rise of the reduced catalyst signal (500 nm, green) in the QDs−cat system, indicating that the positive absorption in this region has contributions from electrons involved in the charge transfer event. We attribute the A2 band specifically to trapped electrons, based on the rise time of the signal. We discard cooling to the band edge states as a likely explanation for the increase in signal magnitude on short time scales, since no corresponding growth is visible on the CB electron induced bleach (B1). Instead, we assign the fast *recovery* component of the B1 band (Figure 2f) to electron trapping. The trapped electrons can subsequently be promoted to CB-related states by probe absorption, resulting in positive features in the visible (i.e., A1 and A2). The kinetics of the A1 band in the presence of the catalyst cannot be evaluated due to the overlapping with the catalyst absorption; however, the similar dynamic behavior of A1 and A2 in the absence of the catalyst indicates their

shared origin. This assignment is consistent with the retained rise and decay times of the positive signals in the visible over all pump wavelengths, which implies the involvement of intermediate states accessible on similar time scales using both bandgap and sub-bandgap excitation energies.

The positive NIR signal, we attribute specifically to trapped holes, overlapping with the positive electron (trap) signal in the lower energy region of the visible spectra. Such NIR transitions have been associated with promoting electrons from the VB to Cu-related localized holes in CIS and Cu-doped QDs.[25,46] This assignment indicates a common origin of the NIR signal with the B2 band, both reflecting the trapped hole population. This interpretation is therefore strengthened by the similar sub-ps kinetics of the two bands, attributed to rapid hole localization (inset of Figure 2f). Herein, we have proposed that the B2 band reflects the pump-induced bleaching of Cu+, with a growth corresponding to the VB-to-Cu+ hole localization kinetics to form the bleached Cu2+-like state. Previous studies, however, have indicated the presence of both Cu+ and Cu2+ in Cu-poor CIS QDs.[27] The NIR TA signal and the B2 band might therefore reflect different subsets of localized holes which, in addition to the overlapping of signals in the visible, can explain the differences in the kinetics of the two bands on longer time scales. The Cu+, in contrast to Cu2+, has to be photoactivated by capturing a hole prior to NIR absorption. Cu2+ ions are instead accompanied by Cu-vacancies, which upon bandgap excitation can accept the photogenerated VB hole.[46] The low amplitude GSA feature observed in the NIR of the present QDs can therefore be an indication of ground state Cu2+, whereas the transient absorption in this region is consistent with transitions involving VB electrons promoted to trapped holes of varying nature but with a rise time likely reflecting the faster VB-to-Cu+ hole localization kinetics.

Decomposition of Transient Spectra. On the basis of the interpretations of the spectral contributions, a model was constructed which is summarized in Figure 7. The colored bands represents a schematic decomposition of the TA spectrum obtained using pump energies related to bandgap transitions. The spectral contributions (a) are summarized in the simplified energy diagram (b). The proposed model involves positive absorption from electron trap states (A1, purple and A2, orange) and contributions associated with transitions of VB electrons to localized holes (vis to NIR, red). The former assignment is evidenced by (i) the faster decay of the A2 band in the presence of the electron scavenger (catalyst) and (ii) the pump wavelength invariant kinetics (rise and decay) of the positive bands. The broad transient absorption in the MIR is associated with electrons in the CB or CB-related states (gray arrow). Importantly, the present model includes two overlapping bleach bands dominated by state filling CB electrons and localized holes (B1, blue and B2, green, respectively). So far, the distinct carrier contributions to the bleach bands are proposed based on the observation of (i) the invariant/variant spectral shifts of the bleach bands using pump wavelengths corresponding to interband/sub-bandgap transitions, (ii) a more long-lived B2 bleach in the presence of the electron scavenger, and (iii) the different dynamical behavior of the B1 and B2 band.

Despite the consistency of our data with schematic b in Figure 6, such a model does not provide an obvious explanation for the decoupled recovery kinetics of the signals assigned to trapped holes (B2) and CB electrons (B1). With
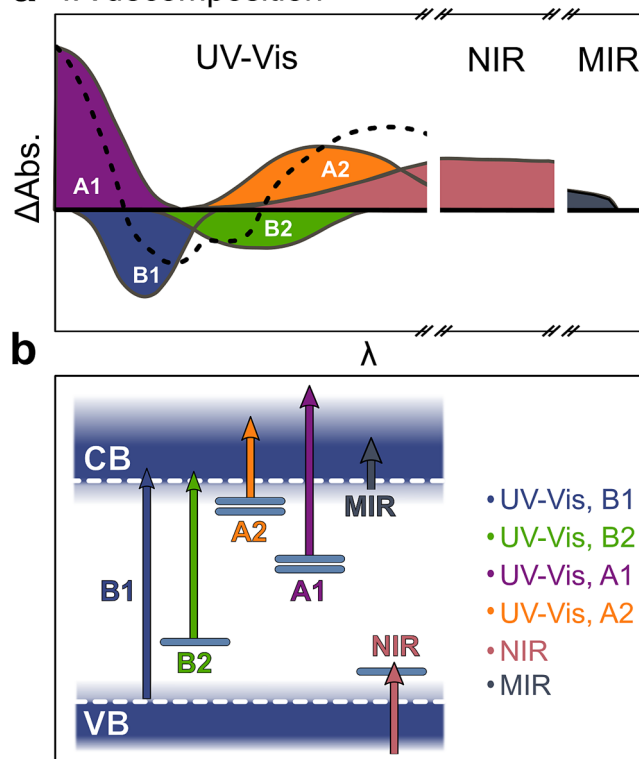

Figure 7. Schematic representations of the discussed contributions to the transient absorption (TA) data. (a) Decomposition of the TA spectra following pump energies related to VB−CB transitions. The dotted line corresponds to the sum of the superimposed signals and represents the experimental TA spectra. (b) Schematic energy diagram showing the transitions involved in the bands of the corresponding color in the decomposed TA spectrum.

the present interpretations, the more short-lived B2 band indicates that the hole population decays rapidly while leaving the long-lived CB electrons unperturbed. Such a behavior is rather unexpected based on the literature, where *long-lived* Cu-localized holes have been shown to function as acceptors in a radiative recombination mechanism. The sensitivity, however, of these holes to other than CB electrons provides a speculative explanation where a subset of trapped electrons are recombining with the bleaching holes on shorter time scales. This is supported by global analysis (Figure 2e), where the τ_1 and τ_2 DAS components show a clear loss of the B2 band as well as of the positive signals in the UV−vis. Furthermore, the isosbestic point at ∼535 nm (inset Figure 2a) suggests that the carriers involved in the A2 feature recombines with the carriers responsible for the B2 band. In the proposed model, this behavior is associated with trapped electrons recombining with the localized holes, likely nonradiatively, consistent with the decoupled recovery kinetics of the B1 and B2 band (Figure 8).

Ultrafast Charge Transfer in Self-Assembled QD-Catalyst Complexes. The utilization of QDs as photosensitizers to molecular (single hole or electron) acceptors has been demonstrated in a large variety of studies through the latest decades. Studies on photocatalytic systems with QDs and molecular catalysts combined are, however, less common.[7,9,10] For molecular catalysts, as acceptors of multiple consecutive charges, the rates of the QD-catalyst charge transfer events are
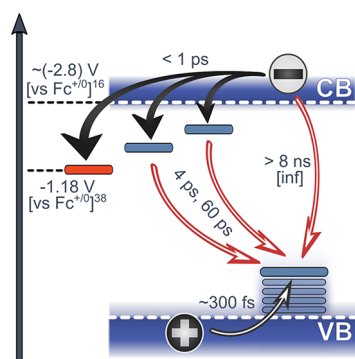
Figure 8. Schematic depiction of the processes involved in the deactivation of photoexcited $Cu_{0.2}In_1S_x$ quantum dots (QDs). The reduction potentials of the QDs and $[Fe_2(cbdt)(CO)_6]$ catalyst are indicated (ref 16 and ref 40) together with the time components obtained from the fitting of transient absorption data. From the energetic difference between the excitonic (~bandgap) maximum and the tail band, the absorption active hole-trap states can be estimated to extend roughly <650 meV above the VB edge.

of great importance to control in order to prevent losses and to allow the catalyst to accumulate the involved redox carriers.

Herein, we show that the photoexcitation of Cu-deficient CIS QDs with a hybrid L-cysteine capping ligand layer results in ultrafast single electron transfer to the $[Fe_2(cbdt)(CO)_6]$ catalyst. Ultrafast electron transfer from excited QDs or molecular dyes is well-established as evidence for the preassociation with the quencher.[48] This is further supported by the enhancement (Figure S8a,b) of the QD PL at low catalyst concentrations (<15 μM) prior to quenching (>15 μM). This PL enhancement is an indication of a strong interaction between the QDs and the catalysts.[49] To gain further insight into the self-association mechanism, we performed quenching experiments comparing the $[Fe_2(cbdt)]$ catalyst with the $[Fe_2(bdt)]$ parent compound (Figure 3b). The results show that the catalysts are efficient PL quenchers, with even better efficiency for the parent compound, indicating that the −COOH group is not responsible for driving the formation of these assemblies. For both catalysts, the quenching is much stronger than possible for diffusion-controlled processes, giving evidence for self-assembly of either catalyst with the QDs.

Huang et al. (2018) observed similar ultrafast charge transfer rates, in CIS QDs covalently linked with a $[Re(bpy)(CO)_3Cl]$ derivative catalyst, by transient absorption probing in the MIR.[15] The ultrafast electron transfer was assigned to the strong electronic coupling between the QDs and the catalyst. A control experiment where the CIS QDs capped with 3-mercaptopropionic acid (3-MPA) simply mixed with the parent $[Re(bpy)(CO)_3Cl]$ catalyst also showed features associated with the reduced catalyst on ultrafast time scales. This is evidence that the catalyst without specific binding motifs was able to associate with the QDs. L-Cysteine and MPA are close relatives, with common coordination sites associated with the carboxylate or thiol side chain. It is possible that these sites, in addition to the amino group of L-cysteine, might be involved in driving the formation of high-affinity complexes in these systems. The small size of these molecules could thus be advantageous compared to more bulky ligands, allowing the charges to transfer efficiently without having to penetrate the ligand shell or exchange with ligands. Weiss and co-workers observed a similar behavior of ultrafast charge

transfer in core/shell CIS/ZnS QDs with a molecular *meso*-tetraphenylporphyrin iron(III) chloride catalyst, a system without organic capping groups. The QD-catalyst complex formation was suggested to be driven by the interaction between surface sulfur atoms on the QDs and the iron of the catalyst.

The experiments performed herein are not sufficient to identify the interactions that drive the self-assembly in the present system, but it is clear that it can provide a great advantage compared to systems relying on bimolecular collision rates or synthetic linking. Efforts to determine charge transfer rates and to characterize the interactions that drive such self-assembly in more detail could therefore benefit the field of artificial photosynthesis relying on efficient charge transfer events and selectivity. The large variety of QD species and surface agents as well as the tunability of molecular catalysts provide a great but challenging opportunity. Controlling the interplay between the QDs and catalyst (dictated by their chemical/physical nature, including QD surface agents) plays a key role for efficient system optimization.

◼ CONCLUSIONS

Fs-TA experiments of Cu-deficient CIS QDs were carried out by selectively pumping at different wavelengths. The transient spectra revealed overlapping bleaching of bandgap (B1) and sub-bandgap (B2) transitions with major contributions from state filling electrons and (trapped) holes, respectively. This model strengthens the picture of dual optical transitions present in CIS QDs, where the compositional stoichiometry plays a crucial role in determining the relative weight of the transitions involved. We note that a trapped hole contribution to the bleach has not been suggested before in the literature; further studies would therefore have to clarify if the behavior typical of the present QDs can be generalized to similar systems. Finally, this study highlights the importance of considering overlapping contributions when assigning charge carrier dynamics in similar systems. This is of great importance considering that the electron and hole dynamics need to be monitored independently for efficient system optimization. Further studies can clarify how the tunability window provided by off-stoichiometric compositions can be utilized to enhance both hole and electron transfer efficiencies to redox partners.

The direct evidence of the singly reduced $[Fe_2(cbdt)(CO)_6]$ catalyst was found by probing in the UV−vis and MIR regions. These experiments revealed a sub-ps electron transfer upon photoexcitation of the QDs, which indicates that the charge transfer is not limited by diffusion rates. Such a behavior suggests that the catalyst adsorbs onto the QD surface prior to photoexcitation. Further characterization and enhancement of such interactions present opportunities for constructing efficient fuel forming systems without relying on advanced synthetic methods.

◼ ASSOCIATED CONTENT

ⓈⒾ Supporting Information

The following files are available as Supporting Information. The Supporting Information is available free of charge at https://pubs.acs.org/doi/10.1021/acs.jpcc.1c02468.

Supporting calculations, Figure S1 showing morphological characterization of $Cu_{0.2}In_1S_x$ QDs with transmission electron microscopy images and powder X-ray

diffraction; Figure S2 showing optical characterization with ground state absorption spectra and time-correlated single photon counting (TCSPC); Figures S3−S6 showing supplementary transient absorption data and fits (UV−vis); Figure S7 showing supplementary transient absorption data (mid-IR, pump, 560 nm) and quantum dots together with catalyst; Figure S8 showing results of quenching experiment; and Tables S1 and S2 listing copper to indium ratio determined through inductively coupled plasma measurements and fitting parameters for transient absorption and TCSPC (PDF)

■ AUTHOR INFORMATION

Corresponding Author

    Leif Hammarström − *Department of Chemistry, Uppsala University, SE 751 20 Uppsala, Sweden;* ⓞ orcid.org/0000-0002-9933-9084; Phone: +46 (0)18 471 3648; Email: Leif.Hammarstrom@kemi.uu.se

Authors

    Nora Eliasson − *Department of Chemistry: Ångström Laboratory, Uppsala University, SE 751 20 Uppsala, Sweden*

    Belinda Pettersson Rimgard − *Department of Chemistry: Ångström Laboratory, Uppsala University, SE 751 20 Uppsala, Sweden*

    Ashleigh Castner − *Department of Chemistry: Ångström Laboratory, Uppsala University, SE 751 20 Uppsala, Sweden;* ⓞ orcid.org/0000-0002-8732-6470

    Cheuk-Wai Tai − *Department of Materials and Environmental Chemistry, Stockholm University, SE 106 91 Stockholm, Sweden;* ⓞ orcid.org/0000-0001-7286-1211

    Sascha Ott − *Department of Chemistry, Uppsala University, SE 751 20 Uppsala, Sweden;* ⓞ orcid.org/0000-0002-1691-729X

    Haining Tian − *Department of Chemistry, Uppsala University, SE 751 20 Uppsala, Sweden;* ⓞ orcid.org/0000-0001-6897-2808

Complete contact information is available at:

https://pubs.acs.org/10.1021/acs.jpcc.1c02468

Notes

The authors declare no competing financial interest.

■ REFERENCES

(1) Balzani, V.; Moggi, L.; Manfrin, M.; Bolletta, F.; Gleria, M. Solar Energy Conversion by Water Photodissociation. *Science* **1975**, *189*, 852−856.

(2) Calvin, M. Solar Energy by Photosynthesis. *Science* **1974**, *184*, 375−381.

(3) Fujishima, A.; Honda, K. Electrochemical Photolysis of Water at a Semiconductor Electrode. *Nature* **1972**, *238*, 37−38.

(4) Lewis, N.; Nocera, D. Powering the planet: Chemical challenges in solar energy utilization. *Proc. Natl. Acad. Sci. U. S. A.* **2006**, *103*, 15729−15735.

(5) Hammarström, L. Artificial photosynthesis: closing remarks. *Faraday Discuss.* **2017**, *198*, 549−56.

(6) Lian, S.; Kodaimati, M.; Weiss, E. Photocatalytically Active Superstructures of Quantum Dots and Iron Porphyrins for Reduction of CO_2 to CO in Water. *ACS Nano* **2018**, *12*, 568−575.

(7) Harris, R.; Bettis Homan, S.; Kodaimati, M.; He, C.; Nepomnyashchii, A.; Swenson, N.; Lian, S.; Calzada, R.; Weiss, E. Electronic Processes within Quantum Dot-Molecule Complexes. *Chem. Rev.* **2016**, *116*, 12865−12919.

(8) Klimov, V. Spectral and Dynamical Properties of Multiexcitons in Semiconductor Nanocrystals. *Annu. Rev. Phys. Chem.* **2007**, *58*, 635−73.

(9) Cheng, M.; Wang, M.; Zhang, S.; Liu, F.; Yang, Y.; Wan, B.; Sun, L. Photocatalytic H_2 production using a hybrid assembly of an [FeFe]-hydrogenase model and CdSe quantum dot linked through a thiolato-functionalized cyclodextrin. *Faraday Discuss.* **2017**, *198*, 197−209.

(10) Wang, F.; Wang, W.-G.; Wang, X.-J.; Wang, H.-Y.; Tung, C.-H.; Wu, L.-Z. A Highly Efficient Photocatalytic System for Hydrogen Production by a Robust Hydrogenase Mimic in an Aqueous Solution. *Angew. Chem., Int. Ed.* **2011**, *50*, 3193−3197.

(11) Hughes, K.; Hartstein, K.; Gamelin, D. Photodoping and Transient Spectroscopies of Copper-Doped CdSe/CdS Nanocrystals. *ACS Nano* **2018**, *12*, 718−728.

(12) Aldakov, D.; Lefrançois, A.; Reiss, P. Ternary and quaternary metal chalcogenide nanocrystals: Synthesis, properties and applications. *J. Mater. Chem. C* **2013**, *1*, 3756−3776.

(13) Ratzloff, M. W.; Wilker, M. B.; Mulder, D. W.; Lubner, C. E.; Hamby, H.; Brown, K. A.; Dukovic, G.; King, P. W. Activation Thermodynamics and H/D Kinetic Isotope Effect of the H_{ox} to $H_{red}H^+$ Transition in [FeFe] Hydrogenase. *J. Am. Chem. Soc.* **2017**, *139*, 12879−12882.

(14) Wu, K.; Chen, Z.; Lv, H.; Zhu, H.; Hill, C. L.; Lian, T. Hole Removal Rate Limits Photodriven H_2 Generation Efficiency in CdS-Pt and CdSe/CdS-Pt Semiconductor Nanorod−Metal Tip Heterostructures. *J. Am. Chem. Soc.* **2014**, *136*, 7708−7716.

(15) Huang, J.; Gatty, M.; Xu, B.; Pati, P.; Etman, A.; Tian, L.; Sun, J.; Hammarström, L.; Tian, H. Covalently linking $CuInS_2$ quantum dots with a Re catalyst by click reaction for photocatalytic CO_2 reduction. *Dalt. Transac.* **2018**, *47*, 10775−10783.

(16) Lian, S.; Kodaimati, M.; Dolzhnikov, D.; Calzada, R.; Weiss, E. Powering a CO_2 Reduction Catalyst with Visible Light through Multiple Sub-picosecond Electron Transfers from a Quantum Dot. *J. Am. Chem. Soc.* **2017**, *139* (26), 8931−8938.

(17) Capon, J.-F.; Gloaguen, F.; Schollhammer, P.; Talarmin, J. Activation of proton by the two-electron reduction of a di-iron organometallic complex. *J. Electroanal. Chem.* **2006**, *595*, 47−52.

(18) Felton, G. A. N.; Vannucci, A. K.; Chen, J.; Lockett, L. T.; Okumura, N.; Petro, B. J.; Zakai, U. I.; Evans, D. H.; Glass, R. S.; Lichtenberger, D. L. Hydrogen Generation from Weak Acids: Electrochemical and Computational Studies of a Diiron Hydrogenase Mimic. *J. Am. Chem. Soc.* **2007**, *129*, 12521−12530.

(19) Pullen, S.; Fei, H.; Orthaber, A.; Cohen, S. M.; Ott, S. Enhanced Photochemical Hydrogen Production by a Molecular Diiron Catalyst Incorporated into a Metal−Organic Framework. *J. Am. Chem. Soc.* **2013**, *135*, 16997−17003.

(20) Chen, Y.; Li, S.; Huang, L.; Pan, D. Green and Facile Synthesis of Water-Soluble Cu-In-S/ZnS Core/Shell Quantum Dots. *Inorg. Chem.* **2013**, *52*, 7819−7821.

(21) Huang, J.; Xu, B.; Tian, L.; Pati, P.; Etman, A.; Sun, J.; Hammarström, L.; Tian, H. A heavy metal-free $CuInS_2$ quantum dot sensitized NiO photocathode with a Re molecular catalyst for photoelectrochemical CO_2 reduction. *Chem. Commun.* **2019**, *55*, 7918−7921.

(22) Jara, D.; Stamplecoskie, K.; Kamat, P. Two Distinct Transitions in Cu_xInS_2 Quantum Dots. Bandgap versus Sub-Bandgap Excitations

in Copper-Deficient Structures. *J. Phys. Chem. Lett.* **2016**, *7*, 1452−1459.

(23) Debnath, T.; Ghosh, H. Ternary Metal Chalcogenides: Into the Exciton and Biexciton Dynamics. *J. Phys. Chem. Lett.* **2019**, *10*, 6227−6238.

(24) Li, L.; Pandey, A.; Werder, D.; Khanal, B.; Pietryga, J.; Klimov, V. Efficient Synthesis of Highly Luminescent Copper Indium Sulfide-Based Core/Shell Nanocrystals with Surprisingly Long-Lived Emission. *J. Am. Chem. Soc.* **2011**, *133*, 1176−1179.

(25) Knowles, K.; Hartstein, K.; Kilburn, T.; Marchioro, A.; Nelson, H.; Whitham, P.; Gamelin, D. Luminescent Colloidal Semiconductor Nanocrystals Containing Copper: Synthesis, Photophysics, and Applications. *Chem. Rev.* **2016**, *116*, 10820−10851.

(26) Nelson, H.; Gamelin, D. Valence-Band Electronic Structures of Cu$^+$-Doped ZnS, Alloyed Cu- In-Zn-S, and Ternary CuInS$_2$ Nanocrystals: A Unified Description of Photoluminescence across Compositions. *J. Phys. Chem. C* **2018**, *122*, 18124−18133.

(27) Fuhr, A.; Yun, H.; Crooker, S.; Klimov, V. Spectroscopic and Magneto-Optical Signatures of Cu^{1+} and Cu^{2+} Defects in Copper Indium Sulfide Quantum Dots. *ACS Nano* **2020**, *14*, 2212−2223.

(28) Li, L.; Daou, T.; Texier, I.; Chi, T. T. K.; Liem, N. Q.; Reiss, P. Highly Luminescent CuInS$_2$/ZnS Core/Shell Nanocrystals: Cadmium-Free Quantum Dots for In Vivo Imaging. *Chem. Mater.* **2009**, *21*, 2422−2429.

(29) Zhang, J.; Sun, W.; Yin, L.; Miao, X.; Zhang, D. One-pot synthesis of hydrophilic CuInS$_2$ and CuInS$_2$−ZnS colloidal quantum dots. *J. Mater. Chem. C* **2014**, *2*, 4812−4817.

(30) Jia, L.; Wang, Y.; Nie, Q.; Liu, B.; Liu, E.; Hu, X.; Fan, J. Aqueous-synthesis of CuInS$_2$ core and CuInS$_2$/ZnS core/shell quantum dots and their optical properties. *Mater. Lett.* **2017**, *200*, 27−30.

(31) Zhang, B.; Wang, Y.; Yang, C.; Hu, S.; Gao, Y.; Zhang, Y.; Wang, Y.; Demir, H.; Liu, L.; Yong, K.-T. The composition effect on the optical properties of aqueous synthesized Cu−In−S and Zn−Cu−In−S quantum dot nanocrystals. *Phys. Chem. Chem. Phys.* **2015**, *17*, 25133−25141.

(32) Yan, R.; Zhang, W.; Wu, W.; Dong, X.; Wang, Q.; Fan, J. Optical spectroscopy reveals transition of CuInS$_2$/ZnS to Cu$_x$Zn$_{1−x}$InS$_2$/ZnS:Cu alloyed quantum dots with resultant double-defect luminescence. *APL Mater.* **2016**, *4*, 126101.

(33) Knowles, K.; Nelson, H.; Kilburn, T.; Gamelin, D. Singlet-Triplet Splittings in the Luminescent Excited States of Colloidal Cu$^+$:CdSe, Cu$^+$:InP, and CuInS$_2$ Nanocrystals: Charge-Transfer Configurations and Self-Trapped Excitons. *J. Am. Chem. Soc.* **2015**, *137*, 13138−13147.

(34) Fuhr, A.; Yun, H.; Makarov, N.; Li, H.; McDaniel, H.; Klimov, V. Light-Emission Mechanism in CuInS$_2$ Quantum Dots Evaluated by Spectral Electrochemistry. *ACS Photonics* **2017**, *4*, 2425−2435.

(35) Zhong, H.; Zhou, Y.; Ye, M.; He, Y.; Ye, J.; He, C.; Yang, C.; Li, Y. Controlled Synthesis and Optical Properties of Colloidal Ternary Chalcogenide CuInS$_2$ Nanocrystals. *Chem. Mater.* **2008**, *20*, 6434−6443.

(36) Jeong, S.; Ko, M.; Jeong, S.; Shin, S. Y.; Park, S. M.; Do, Y. R.; Song, J. K. Optical Transitions of CuInS$_2$ Nanoparticles: Two Types of Absorption and Two Types of Emission. *J. Phys. Chem. C* **2020**, *124*, 14400−14408.

(37) Jiao, M.; Huang, X.; Ma, L.; Li, Y.; Zhang, P.; Wei, X.; Jing, L.; Luo, X.; Rogach, A.; Gao, M. Biocompatible off-stoichiometric copper indium sulfide quantum dots with tunable near-infrared emission via aqueous based synthesis. *Chem. Commun.* **2019**, *55*, 15053−15056.

(38) Chen, B.; Zhong, H.; Zhang, W.; Tan, Z.; Li, Y.; Yu, C.; Zhai, T.; Bando, Y.; Yang, S.; Zou, B. Highly Emissive and Color-Tunable CuInS$_2$-Based Colloidal Semiconductor Nanocrystals: Off-Stoichiometry Effects and Improved Electroluminescence Performance. *Adv. Funct. Mater.* **2012**, *22*, 2081−2088.

(39) Pavlishchuk, V. V.; Addison, A. W. Conversion constants for redox potentials measured versus different reference electrodes in acetonitrile solutions at 25°C. *Inorg. Chim. Acta* **2000**, *298*, 97−102.

(40) Brown, A. M.; Antila, L. J.; Mirmohades, M.; Pullen, S.; Ott, S.; Hammarström, L. Ultrafast Electron Transfer Between Dye and Catalyst on a Mesoporous NiO Surface. *J. Am. Chem. Soc.* **2016**, *138*, 8060−8063.

(41) Mirmohades, M.; Pullen, S.; Stein, M.; Maji, S.; Ott, S.; Hammarström, L.; Lomoth, R. Direct Observation of Key Catalytic Intermediates in a Photoinduced Proton Reduction Cycle with a Diiron Carbonyl Complex. *J. Am. Chem. Soc.* **2014**, *136*, 17366−17369.

(42) Sa, J.; Pavliuk, M.; Cieślak, A.; Abdellah, M.; Budinská, A.; Pullen, S.; Sokołowski, K.; Fernandes, D.; Szlachetko, J.; Bastos, E.; et al. Hydrogen Evolution with Nanoengineered ZnO Interfaces Decorated by a Beetroot Extract and a Hydrogenase Mimic. *Sustain Energy Fuels* **2017**, *1*, 69−73.

(43) Sun, J.; Zhu, D.; Zhao, J.; Ikezawa, M.; Wang, X.; Masumoto, Y. Ultrafast carrier dynamics in CuInS$_2$ Quantum Dots. *Appl. Phys. Lett.* **2014**, *104*, 023118.

(44) Grimaldi, G.; Geuchies, J.; van der Stam, W.; du Fossé, I.; Brynjarsson, B.; Kirkwood, N.; Kinge, S.; Siebbeles, L.; Houtepen, A. Spectroscopic Evidence for the Contribution of Holes to the Bleach of Cd-Chalcogenide Quantum Dots. *Nano Lett.* **2019**, *19*, 3002−3010.

(45) Chen, W.; Qi, J.; Dong, C.; Chen, J.; Shen, Z.; He, Y.; Yang, S.; Chen, T.; Chen, C.; Li, Y.; et al. Solution-Processed in Situ Growth of CuInS$_2$ Nanoparticle Films for Efficient Planar Heterojunction Solar Cells with a Dual. *ACS Appl. Energy Mater.* **2019**, *2*, 5231−5242.

(46) Berends, A.; Rabouw, F.; Spoor, F.; Bladt, E.; Grozema, F.; Houtepen, A.; Siebbeles, L.; de Mello Donegá, C. Radiative and Nonradiative Recombination in CuInS$_2$ Nanocrystals and CuInS$_2$-Based Core/Shell Nanocrystals. *J. Phys. Chem. Lett.* **2016**, *7* (17), 3503−3509.

(47) Zhou, Y.; Hu, W.; Ludwig, J.; Huang, J. Exceptionally Robust CuInS$_2$/ZnS Nanoparticles as Single Component Photocatalysts for H$_2$ Evolution. *J. Phys. Chem. C* **2017**, *121*, 19031−19035.

(48) Lakowicz, J. R. *Principles of Fluorescence Spectroscopy*, 3rd ed.; Springer: New York, 2006; pp 278−285.

(49) Ye, Y.; Xu, Y.; Huang, L.; Fan, D.; Feng, Z.; Wang, X.; Li, C. Roles of adsorption sites in electron transfer from CdS quantum dots to molecular catalyst cobaloxime studied by time-resolved spectroscopy. *Phys. Chem. Chem. Phys.* **2016**, *18*, 17389−17397.